

1 Solar wind driven variations of electron plasma sheet
2 densities and temperatures beyond geostationary
3 orbit during storm times

S. Dubyagin¹, N. Yu. Ganushkina^{1,2}, I. Sillanpää¹, A. Runov³

Corresponding author: S. Dubyagin, Finnish Meteorological Institute, POBox 503, Helsinki,
FIN-00101, Finland/(Stepan.Dubyagin@fmi.fi)

¹Finnish Meteorological Institute,
Helsinki, Finland.

²Climate and Space Sciences and
Engineering Department, University of
Michigan, Ann Arbor, MI, USA.

³Institute of Geophysics and Planetary
Physics, University of California,
Los Angeles, USA.

This is the author manuscript accepted for publication and has undergone full peer review but has not been through the copyediting, typesetting, pagination and proofreading process, which may lead to differences between this version and the Version of Record. Please cite this article

as doi:10.1002/2016JA022947 August 18, 2016, 1:10am

D R A F T

Abstract. The empirical models of the plasma sheet electron temperature and density on the nightside at distances between 6 and 11 R_E are constructed based on Time History of Events and Macroscale Interactions During Substorms (THEMIS) particle measurements. The data set comprises ~ 400 hours of observations in the plasma sheet during geomagnetic storm periods. The equatorial distribution of the electron density reveals a strong earthward gradient and a moderate variation with magnetic local time symmetric with respect to the midnight meridian. The electron density dependence on the external driving is parameterized by the solar wind proton density averaged over 4 hours and the southward component of interplanetary magnetic field (IMF B_S) averaged over 6 hours. The interval of the IMF integration is much longer than a typical substorm growth phase and it rather corresponds to the geomagnetic storm main phase duration. The solar wind proton density is the main controlling parameter but the IMF B_S becomes of almost the same importance in the near-Earth region. The root-mean-square deviation between the observed and predicted plasma sheet density values is 0.23 cm^{-3} and the correlation coefficient is 0.82. The equatorial distribution of the electron temperature has a maximum in the post-midnight – morning MLT sector, and it is highly asymmetric with respect to the local midnight. The electron temperature model is parameterized by solar wind velocity (averaged over 4 hours), IMF B_S (averaged over 45 min), and IMF B_N (northward component of IMF, averaged over 2 hours). The solar wind velocity is a major controlling parameter and IMF B_S and B_N are compara-

27 ble in importance. In contrast to the density model, the electron tempera-
28 ture shows higher correlation with the IMF B_S averaged over ~ 45 min (sub-
29 storm growth phase time scale). The effect of B_N manifests mostly in the
30 outer part of the modelled region ($r > 8R_E$). The influence of the IMF B_S
31 is maximal in the midnight – post-midnight MLT sector. The correlation co-
32 efficient between the observed and predicted plasma sheet electron temper-
33 ature values is 0.76 and the root-mean-square deviation is 2.6 keV. Both mod-
34 els reveal better performance in the dawn MLT sector.

Author Manuscript

1. Introduction

35 The distributions of low energy electrons (below 200-300 keV) and their variations in the
36 near-Earth plasma sheet, at distances beyond geostationary orbit, have not sufficiently
37 been studied in detail. Yet, this population is critically important for magnetospheric
38 dynamics, especially during storm times. One obvious example is their role as the seed
39 population, being further accelerated to MeV energies by various processes in the Earth's
40 radiation belts. Several modeling attempts have been made [*Jordanova and Miyoshi, 2005;*
41 *Miyoshi et al., 2006; Chen et al., 2006; Jordanova et al., 2014*]. The electron flux at these
42 low energies is largely determined by convective and substorm-associated electric fields and
43 varies significantly with geomagnetic activity driven by the solar wind [*Mauk and Meng,*
44 *1983; Kerns et al., 1994; Liemohn et al., 1998; Ganushkina et al., 2013, 2014*]. Inward
45 electron transport includes also radial diffusion and excites plasma wave instabilities that
46 give rise to local electron acceleration and electron precipitation into the atmosphere.
47 Transport and loss processes are far from being understood at present. It should be also
48 noted that the electron flux at these energies is important for spacecraft surface charging
49 [*Garrett, 1981; Lanzerotti et al., 1998; Davis et al., 2008; Thomsen et al., 2013*].

50 There has been a number of studies on low energy electrons at geostationary orbit.
51 *Korth et al. [1999]; Denton et al. [2005]; Sicard-Piet et al. [2008]; Denton et al. [2015]*
52 concentrated mainly on the analysis of LANL MPA and SOPA electron data. *Friedel et*
53 *al. [2001]* analyzed the electron data from the Polar Hydra instrument and *Kurita et al.*
54 *[2011]* the data from the THEMIS spacecraft. None of the studies produced solar wind

55 driven empirical relations for electron fluxes or moments of electron distribution function
56 which can be used easily for radiation belt modeling.

57 In the near-Earth plasma sheet, continuous measurements of plasma sheet electrons
58 are not available, in contrast to geostationary orbit. Numerous studies addressed the
59 magnetospheric plasma transport and sources [*Terasawa et al.*, 1997; *Borovsky et al.*,
60 1998a, b; *Wind and Newell*, 2002]. There have been several statistical models for plasma
61 sheet electrons derived from GEOTAIL and CLUSTER data, such as, for example, *Åsnes*
62 *et al.* [2008]; *Burin des Rozières et al.* [2009]. *Artemyev et al.* [2013] analyzed the electron
63 temperature radial distribution in the magnetotail using THEMIS observations at $r >$
64 $10R_E$. These studies are not models with empirical relations which can be used for real
65 event modeling by the wider scientific community.

66 Only two empirical models of the plasma sheet plasma parameters have been presented
67 since 2000. These models are *Tsyganenko and Mukai* [2003] and *Sergeev et al.* [2015]. The
68 *Tsyganenko and Mukai* [2003] model is the only model, where an analytical description of
69 the plasma parameters derived for a 2D distribution of the central plasma sheet ion temperature
70 T_i , density n_i and pressure p_i as functions of the incoming solar wind and interplanetary
71 magnetic field parameters at distances of 10-50 R_E based on Geotail data. *Sergeev et*
72 *al.* [2015] presented the correlations between 1-h-averaged central plasma sheet and solar
73 wind (and AL index) parameters based on THEMIS data but they were not derived for
74 storm times.

75 *Ganushkina et al.* [2013, 2014, 2015] modeled the electron transport from the plasma
76 sheet to the geostationary orbit setting the boundary at 10 R_E as a kappa distribution
77 with the parameters of number density n_e and temperature T_e in the plasma sheet given

78 by *Tsyganenko and Mukai* [2003]. In *Ganushkina et al.* [2013, 2014, 2015], the electron n_e
79 is assumed to be the same as that for ions and $T_e/T_i = 0.2$ is taken into account (which
80 relation was shown, for example, in *Kaufmann et al.* [2005] and *Wang et al.* [2012], based
81 on Geotail and THEMIS data). A time shift of 2 h following *Borovsky et al.* [1998b] for
82 the solar wind material to reach the midtail plasma sheet is also introduced. Applying
83 *Tsyganenko and Mukai* [2003] model for boundary conditions for electrons has a number
84 of serious limitations. This model was derived from Geotail data for ions. According to
85 the studies based on THEMIS data analysis [*Wang et al.*, 2012], the ratio T_e/T_i can vary
86 during disturbed conditions. Moreover, at distances closer than $10 R_E$, it can happen
87 that the correlation between T_i and T_e does not exist at all and no certain ratio can be
88 determined [*Kunov et al.*, 2015].

89 The paper presents the empirical model of the electron plasma sheet densities and
90 temperatures derived from the THEMIS [*Angelopoulos*, 2008a] data. Sections 2 and 3
91 contain the detailed description of the data we have selected and analyzed. Section 4
92 demonstrates the methodology of determining the model input parameters. Section 5
93 presents the empirical relations for electron plasma sheet density and temperature. The
94 results of the study are discussed in Section 6. The goal of Section 7 is to validate the
95 model performance and Section 8 presents the conclusions.

2. The Data Sources

96 This study relies on the data of the Time History of Events and Macroscale Inter-
97 action during Substorms (THEMIS) mission [*Angelopoulos*, 2008a]. The mission was
98 launched on February 17, 2007, and it comprises five identical probes on elliptical, nearly-
99 equatorial orbits. Each of the probes has among other scientific instruments two particle

100 instruments, namely, Electrostatic Analyser (ESA) [McFadden *et al.*, 2008a] to measure
101 the ion and electron distribution functions over the energy range from a few eV up to
102 25 (30) keV for ions (electrons) on each spin period (~ 3 sec.) and Solid State Telescope
103 (SST) [Angelopoulos *et al.*, 2008b] to measure ion and electron distributions over energies
104 from 25 eV up to first MeVs on each spin period. We also used the spin resolution
105 Flux Gate Magnetometer (FGM) data [Auster *et al.*, 1991]. All aforementioned data
106 and the calibrating procedures are publicly available at the THEMIS mission web site
107 (<http://themis.ssl.berkeley.edu/index.shtml>)

108 In this study we used solar wind and IMF data from the OMNI database from the
109 GSFC/SPDF OMNIWeb interface at <http://omniweb.gsfc.nasa.gov>. 5-min. resolution
110 data were used as input parameters for magnetotail neutral sheet model [Tsyganenko
111 and Fairfield, 2004] and 1-min. resolution data were used for computation of the input
112 parameters for our empirical model of electron temperature and density.

113 Finally, the 1-min. resolution SYM-H index was downloaded from World Data Center
114 for geomagnetism, Kyoto (<http://wdc.kugi.kyoto-u.ac.jp/>).

3. Selection of data intervals

115 We have analyzed the data from the particle detectors onboard the THEMIS probes
116 P3, P4, P5 (D, E, A) during geomagnetic storms which took place through 2007–2013.
117 All observations came from the region on the nightside at distances $r = 6\text{--}11 R_E$. The
118 major axes of the orbits for all probes were aligned so that the probes were clustered
119 closely during their apogees at $r = 10\text{--}12 R_E$. However, in this study we did not use
120 the advantage of a multi-spacecraft mission and consider the measurements at different

121 spacecraft as independent data records. The probe separation in this region was typically
122 $\sim 0.03\text{--}2R_E$ except for year 2013 when the separation varied between 2 and $8R_E$.

123 Storm periods were of a special interest for our study, since the solar wind driving
124 as well as the magnetospheric plasma parameters can reach extreme values and all the
125 dependencies as well as their saturation levels can manifest more clearly. For this reason,
126 we selected all the periods with $SYM - H < -50$ nT and one day before and one day
127 after these periods for almost whole THEMIS mission lifetime 2007–2013. This selection
128 also includes the quiet periods before the storms.

129 When studying the distribution of the plasma parameters in the equatorial plane, it
130 is important to make sure that a probe was in very center of the plasma sheet (near
131 the magnetotail current neutral sheet) to refer the measurements to a particular radial
132 distance. To control the spacecraft position relative to the neutral sheet we use two step
133 selection: (1) Select all periods when the probes are within $1.5 R_E$ from the neutral
134 sheet predicted by *Tsyganenko and Fairfield* [2004] model; (2) Using THEMIS magnetic
135 field measurements we select only measurements when $|B_n| > |B_t|$, where B_n and B_t
136 are the magnetic field components normal and tangential to the model neutral sheet.
137 Such approach is very robust and it has been successfully applied to the THEMIS data
138 [*Dubyagin et al.*, 2010]. This selection procedure was applied to THEMIS data when
139 P3, P4, P5 (D, E, A) probes were at $R = 6\text{--}11R_E$.

140 Although the combined distribution function covers the energy range up to 3 MeV, we
141 only used the data in the 30 eV – 300 keV energy range. The 30 eV low energy limit is
142 chosen so as to eliminate the possible contribution of photoelectrons in case the space-
143 craft potential is evaluated incorrectly. The electron and ion moments were computed

144 from combined (ESA and SST) distribution function using updated calibration proce-
145 dures (including ESA background contamination and SST sun contamination removal,
146 software version dated December 2015). However, even after all calibration procedures
147 are applied, the penetrating background may not be fully removed. As an additional test
148 of the data accuracy, we compare the densities measured by the ion and electron detec-
149 tors. The readers are referred to *McFadden et al.* [2008b] for more details on the ESA
150 performance issues.

151 Depending on ESA and SST mode, the combined plasma moments are available at spin
152 resolution or only at ~ 96 second resolution. When the 3-second resolution moments
153 were available, it was convenient to average them over 96 sec intervals (1.6 minute) to get
154 combined data set with uniform time resolution. It should be noted that the measurements
155 at 96-sec resolution were not accumulated values but instant distributions (accumulated
156 during one spacecraft spin period). For this reason, these data are expected to reveal
157 more scatter and we do not use them for model construction. This data set was used only
158 for verification of the models.

159 After synchronization with the solar wind data, we obtained $\sim 83,000$ data records
160 with ~ 1.6 min resolution $\sim 63,000$ of which are obtained from the spin-resolution data.
161 Since the quasi-neutrality holds in the magnetospheric plasma, the quality of the plasma
162 moments can be checked comparing the densities computed from electron (N_e) and ion
163 (N_i) measurements. It turned out that significant part of the data shows discrepancies
164 between N_e and N_i . In majority of these anomalous events, N_i exceeds N_e . We analyzed
165 these events and found that typically cold dense plasma with energies ≤ 100 eV can be seen
166 right above the low energy limit. It is likely that some part of this cold population is cut

167 off by low energy limit and the fraction of the cut off population is different for the ion and
168 electron distributions. This leads to discrepancy between N_e and N_i measurements. We
169 also found that a vast majority of these events occurred in the 18–24 MLT sector during
170 the periods with very weak geomagnetic activity. This finding is also in agreement with
171 our hypothesis because a cold plasma of the plasmasphere can extend to larger geocentric
172 distances during such periods especially in the dusk-to-midnight sector. Although these
173 data potentially can be used in the future studies, if the presence of multiple populations
174 in the particle distribution is properly addressed, in the present study we discard all
175 measurements which do not satisfy the condition $N_i/1.5 < N_e < 1.5N_i$. This procedure
176 reduced the size of our statistics by one third. Although this criterion seems to be rather
177 weak, it is justified because, during storm time, the ion data are expected to be less
178 accurate in comparison to the electron data due to a contamination from heavier ions and
179 larger gap between ESA and SST energy ranges (especially for late years).

180 Finally, our data set consists of $\sim 45,000$ records obtained from the spin resolution mea-
181 surements and $\sim 12,000$ obtained from ~ 1.6 -min resolution measurements. Hereafter,
182 we will refer to these data sets as a "primary" and "auxiliary" data sets, respectively.
183 Table 1 shows the number of samples in the data sets for every year during the THEMIS
184 mission. The primary data set includes only data starting from the year 2010 while the
185 years 2007–2009 contribute 20% to the auxiliary data set. Figure 1a shows the distri-
186 bution of the points corresponding to the primary data set in the XY_{GSM} plane (only
187 every tenth point is shown). The colors correspond to different SYM-H index ranges. The
188 strong dusk-dawn asymmetry can be seen in the figure. Although moderate asymmetry
189 existed in the original data set (probably owing to orbital/seasonal effect), so promi-

190 nent lack of the data points in the dusk sector is mostly due to removal of the data with
191 $N_i \neq N_e$. Though not immediately obvious from this dense distribution of points, the
192 dawn-dusk asymmetry exists only for the moderate SYM-H subsets and disappears for
193 SYM-H < -50 nT.

194 It is worth comparing these datasets with datasets used in the previous studies. *Tsyga-*
195 *nenko and Mukai* [2003] used Geotail data and their dataset comprised 7234 1-min records
196 (~ 120 hours). Since we used 1.6-min resolution data, the size of our dataset should be
197 multiplied by factor 1.6 to compare with *Tsyganenko and Mukai* [2003] dataset. However,
198 we used observations onboard three probes clustered closely. For this reason, the size of
199 our dataset should be divided by 3 (this estimate is a bit pessimistic because the probe
200 separation can be as large as $\sim 9R_E$). After this normalization, our dataset size corre-
201 sponds to ~ 400 hours of observations. *Wang et al.* [2006] apparently used the same data
202 set as *Tsyganenko and Mukai* [2003]. *Sergeev et al.* [2015] use 4500–5000 hourly averaged
203 measurements onboard three THEMIS probes on the nightside 21–06 MLT $r = 9–12R_E$.
204 After dividing by 3, to take into account simultaneous measurements at three probes, the
205 data set size is 1500–1600 h, which is four times larger than data set used in the present
206 study. However, *Sergeev et al.* [2015] use only data from ESA spectrometer in 5 eV–25 keV
207 energy range and there is no spatial dependence included in the model.

4. Solar wind driven model for electron plasma sheet densities and temperature: Input parameters

4.1. Methodology

208 The macroscopic plasma parameters in the near-Earth magnetotail are affected by
209 multiple factors. Among them, there are the magnetic configuration change (it affects

210 the plasma parameters through the adiabatic compression of the magnetic flux tubes)
211 [*Borovsky et al.*, 1998b; *Dubyagin et al.*, 2010; *Artemyev et al.*, 2013], the substorm cycle
212 (arrival of a new hot tenuous plasma from the distant magnetotail during the main phase)
213 [*Sergeev et al.*, 2015], the variations of the magnetosheath plasma parameters (since the
214 magnetosheath is a source of the plasma sheet material) [*Terasawa et al.*, 1997; *Borovsky*
215 *et al.*, 1998a; *Wang et al.*, 2010], and the variation of the magnetotail plasma transport
216 modulated by the dayside reconnection rate. To make it even more complicated, the
217 regions and mechanisms of the magnetosheath plasma penetration into the magnetotail
218 are different during periods of southward and northward IMF [*Wang et al.*, 2010]. In
219 addition, all these factors affect the plasma sheet with different time lags and these delays
220 can be different for different regions of the magnetotail [*Terasawa et al.*, 1997; *Borovsky*
221 *et al.*, 1998a; *Wang et al.*, 2010]

222 To investigate the lag of the solar wind influence, every record of the plasma sheet
223 electron density and temperature was accompanied by solar wind data containing 12 hour
224 prehistory. In the OMNI database, the solar wind parameters are projected in time to
225 the moment when solar wind reaches the estimated bow shock position. We estimate the
226 shortest time for solar wind disturbance (seen in the OMNI data) to have an effect on
227 the nightside inner magnetosphere to be ~ 5 minutes. For every measurements in the
228 plasma sheet taken at time t_0 , the 12 hours period preceding the time $t_0 - 5$ min. was
229 broken into 15 minute subintervals and solar wind parameters were averaged over these
230 subintervals. That is, every measurement in the plasma sheet was complemented by 48
231 of 15-min averages of the solar wind parameters for the preceding 12 h interval.

As a first step, we binned the THEMIS observations according to the probe location in the plasma sheet. We used two discriminating parameters: a geocentric distance $r = (X^2 + Y^2 + Z^2)^{\frac{1}{2}}$ and an azimuth angle $\phi = \arctan(-Y_{GSM}/X_{GSM})$. We used two intervals of geocentric distance: $r = 6-8.5R_E$ and $r = 8.5-11R_E$, and three sectors of the azimuth angle: dawnside ($-90^\circ < \phi < -30^\circ$), central ($-30^\circ < \phi < 30^\circ$), and duskside ($30^\circ < \phi < 90^\circ$). These bins are shown in Figure 1b. We investigated the dependence of the electron plasma parameters on the solar wind parameters separately for each bin. Let P_k be a plasma sheet parameter and D_{ik} be a 15-min average of a solar wind parameter. Here k is the index corresponding to the plasma sheet measurements at the time t_k and $i = 1, \dots, 48$ corresponds to the 15-min average preceding the time t_k by $\Delta t = 5 \text{ min} + i \cdot 15 \text{ min}$.

For $L = 1, \dots, 48$ and for $M \leq 48 - L + 1$, we computed the following mean sums:

$$F(L, M, k) = \frac{\sum_{i=L}^{L+M-1} D_{ik}}{M}. \quad (1)$$

Here L represents the lag and M represents the duration over which the parameter is averaged.

These sums are equivalent to time integrals:

$$F(t_{lag}, \Delta T, t_k) = \frac{1}{\Delta T} \int_{t_k - t_{lag} - \Delta T}^{t_k - t_{lag}} D(t) dt. \quad (2)$$

The delays of the plasma sheet parameter response to the changes of the solar wind can be deduced from the analysis of the correlation coefficient between P_k and $F(L, M, k)$ for different L and M . These correlation coefficients can be plotted as function of L and M converted to the time units t_{lag} and ΔT .

Imagine an ideal system whose parameter P responds to the changes of some other parameter D with a fixed time lag t_r . The correlation between P and D would have a peak at $t_{lag} = t_r$ and $\Delta T = 0$. However, the correlation would still be high for nonzero ΔT as long as t_r is inside the interval of averaging ($t_{lag} < t_r < t_{lag} + \Delta T$) and ΔT is less than the autocorrelation time scale (T_{auto}) for D (that is, if an instant value of D can be approximated by its mean average over the time interval ΔT). The shaded area in Figure 2 shows the region satisfying the aforementioned conditions. Obviously, inside this region the correlation is highest when the interval of averaging is centered at t_r , that is $t_{lag} + \Delta T/2 = t_r$ (blue dashed line in Figure 2).

However, the parameters of the system do not necessarily depend on instant values (even if lagged) of the external drivers. For example, the magnetic flux in the magnetotail lobes better correlates with the time integrated solar wind geoeffective electric field than with its instant value [Shukhtina *et al.*, 2005]. In such a case, one can expect that correlation would be higher at some $\Delta T > 0$. In addition, in real magnetosphere the time lags obviously are not constant. It also leads to smearing out the correlation peak at $\Delta T = 0$ and an increase of the correlation at $\Delta T > 0$.

4.2. Input parameters for electron plasma sheet density model

Figure 3 shows the plots for correlation between the plasma sheet and the solar wind densities (all results in Sections 4.2–5 are obtained using primary data set). Figures 3a–f correspond to six spatial bins shown in Figure 1b. The horizontal axis corresponds to the time lag or index L in Equation 1. The vertical axis corresponds to the interval of averaging or index M in Equation 1. A color scale on the right side of each plot shows

273 the range of the linear correlation coefficients (C.C.). The black oblique lines correspond
 274 to $\Delta T_N = \text{const} - 2 \cdot t_N$ dependence (equivalent to blue dashed line in Figure 2).

275 There is an obvious similarity between these plots and Figure 2. The correlation max-
 276 ima in Figures 3a, b, c, d are roughly organized along oblique lines, and the regions of
 277 enhanced correlation are delineated by lines $\Delta T_N = \text{const} - t_N$ on the left/bottom side
 278 in Figures 3a, c, d, f.

279 The plots on the left and right correspond to the dawn and dusk bins, respectively. It
 280 can be seen that the maximum correlation is found for the dawnside bins (C.C. ≥ 0.70) and
 281 the correlation is higher for the outer bins (BIN 1–3 see Figure 1b). These results are in
 282 agreement with dusk-dawn asymmetry of the plasma transport from the magnetosheath
 283 found by *Wang et al.* [2005] and *Wang et al.* [2010], however, it is a bit counterintuitive
 284 taking into account the eastward direction of the electron magnetic drifts. The lag values
 285 are generally in agreement with those found by *Borovsky et al.* [1998a].

286 Table 2 presents the statistical properties of the data subsets for the different bins. First
 287 three lines represent the bin numeration and the coordinates. Forth line shows the number
 288 of 1.6-min resolution records in every bin. It can be seen that the most sparsely populated
 289 bin is BIN 6. Its data set comprises 2295 records. However, this number is misleading
 290 since the time-scales of the solar wind parameters variations are much longer than 1.6-min
 291 resolution of our data set. *Borovsky et al.* [1998a] obtained the following characteristic
 292 times-scales: 1.5 h for IMF B_Z , ~ 10 h for solar wind density, and ~ 32 h for solar wind
 293 velocity (these scales are expected to be somewhat shorter for storm periods). To evaluate
 294 the size of our statistics more realistically, we searched through the database, counting
 295 separate 1-hour intervals containing at least one data point. We found 444 such intervals

296 for BIN 1 and 133 intervals for BIN 6. For 5-hour characteristic period, we found 181
 297 intervals for BIN 1 and only 77 intervals for BIN 6. For this reason (and may be partly
 298 due to orbital/seasonal effect), the standard deviations of the solar wind parameters also
 299 show some variations from bin to bin. Bottom part of Table 2 shows the ranges of the
 300 standard deviations found for various lag values between 0 and 12 hours (the standard
 301 deviations were computed for 15-min resolution data). It can be seen that the variability
 302 of the solar wind parameters changes significantly for different time lag values inside a
 303 data subset for a single bin. It means that some dependencies seen in Figure 3 could be
 304 due to a limited size of the dataset since one can expect that the correlation between two
 305 quantities depends on the variability of the driving one. To rule out this possibility, we
 306 plotted additional figures (not shown) in the same format as Figure 3 but for a standard
 307 deviation (σ) of a corresponding solar wind parameter. Analyzing these figures, we found
 308 that the main features seen in Figures 3 are real (σ shows no or weak variation in that
 309 part of the figure).

310 Although the values of ΔT_N and t_N corresponding to the highest correlation obviously
 311 are different from bin to bin, we need to choose fixed values for a computation of the
 312 input parameters for the empirical models. We attempted to find a compromise so that
 313 the model works for all MLTs in $r = 6\text{--}11R_E$ range. Keeping this in mind, $t_N = 0.5$ h
 314 and $\Delta T_N = 4$ h were chosen. These values are marked by a black circle in all panels
 315 of Figure 3. However, it should be remembered that the confidence interval of these
 316 parameters is very broad (at least ± 1 hour).

317 The model dependence on IMF is parameterized by southward (B_S) and northward
 318 (B_N) IMF components ($B_S = -B_Z^{IMF}$ if $B_Z^{IMF} < 0$ and $B_S = 0$ if $B_Z^{IMF} \geq 0$; $B_N = 0$

319 if $B_Z^{IMF} < 0$ and $B_N = B_Z^{IMF}$ if $B_Z^{IMF} \geq 0$). Figure 4 shows the plots of correlations
 320 between the plasma sheet electron density and IMF B_S . The format is the same as in
 321 Figure 3. In contrast to the solar wind density, the highest correlation between the B_S
 322 and plasma sheet electron density is found for the near-Earth bins. Surprisingly, highest
 323 correlations are found for relatively long intervals of averaging $\Delta T_{BS} = 2-6$ h. This is
 324 much longer than typical substorm growth phase duration. It could be due to strong
 325 variations of the lag in the real system, but in such a case one would expect weaker
 326 correlation. We will discuss the possible reasons for this in Section 7. We chose the
 327 $t_{BS} = 0.5$ h and $\Delta T_{BS} = 6$ h. The lag was chosen so to be the same as that for solar wind
 328 density parameter (and it will be shown later that 0.5 h lags are reasonable choice for all
 329 temperature model parameters too).

330 Table 3 summarizes the results presented in this section. When comparing the top
 331 and bottom parts of the Table 3, it can be seen that introducing a time lag to the
 332 input parameter can significantly improve the correlations. We have also checked a few
 333 more solar wind and IMF parameters (not shown). However, even if the correlations
 334 were comparable to those for N_{SW} , B_S and B_N , the resulting model quality (gauged by
 335 correlation between the model predictions and the data, see Section 7) was worse and
 336 we discarded them in the present version of the model. For example, motivated by the
 337 fact that the solar wind - magnetotail plasma transport characteristic time is different for
 338 the intervals southward and northward IMF B_Z , we introduced two parameters $N_{SW}^{(S)}$ and
 339 $N_{SW}^{(N)}$. $N_{SW}^{(S)} = N_{SW}$ when IMF $B_Z < 0$ and $N_{SW}^{(S)} = 0$ when IMF $B_Z > 0$. $N_{SW}^{(N)}$ is defined
 340 in an opposite way. Although the lag-duration plots for $N_{SW}^{(S)}$ and $N_{SW}^{(N)}$ showed plausible
 341 patterns, the resulting quality of the electron density model was worse.

342 It can be noticed that northward component of IMF shows a bit worse correlation
 343 with the plasma sheet density than southward component (Table 3). It turned out that
 344 discarding IMF B_N from the list of input parameters leads to only minor reduction of the
 345 density model quality. For this reason, and for the sake of simplicity, we have left only
 346 two input parameters N_{SW} and B_S in our density model.

4.3. Input parameters for electron plasma sheet temperature model

347 Table 4 shows the correlation between the plasma sheet electron perpendicular temper-
 348 ature (T_e) and solar wind parameters. It can be seen that solar wind velocity exhibits
 349 strongest correlation. Similar results have been found for plasma sheet ion temperature
 350 [Borovsky *et al.*, 1998a; Tsyganenko and Mukai, 2003]. The lowest correlations are ob-
 351 tained for the duskside bins. It can also be noticed that IMF B_S and B_N affect the electron
 352 temperature in an opposite way. Figure 5 shows the correlations between T_e and V_{SW} for
 353 six spatial bins in the same format as in Figure 3. The correlations show very weak de-
 354 pendence on t_V and ΔT_V for several bins. It is an expected result since the solar wind
 355 velocity autocorrelation characteristic time scale is largest of all solar wind parameters
 356 (See Figure 6 in Borovsky *et al.* [1998a]). We chose $t_V = 0.5$ h and $\Delta T_V = 4$ h.

357 Figure 6 shows the similar correlation plots for IMF B_S . There is no clear dependence
 358 on MLT. Although for some bins the correlation is rather weak, the duration and the
 359 lag at the correlation peak fit well the substorm timescales (0.5–2 hours). We chose the
 360 time lag $t_{BS} = 30$ minutes which can be interpreted as the time needed for the lobe
 361 magnetic flux to start to influence the near-Earth magnetotail and the averaging interval
 362 $\Delta T_{BS} = 45$ minutes is close to the typical substorm growth phase duration.

363 Figure 7 shows the similar plots for IMF B_N . Color scale on the right side of each plot
 364 corresponds to the absolute value of the correlation coefficient. The highest correlation
 365 is on the dawnside. Surprisingly, the correlations are even higher than those for B_S . To
 366 make sure that these correlations are not due to the mutual correlation between IMF B_N
 367 and V_{SW} , we inspected the correlation between B_N and V_{SW} for various lags t_V and t_{BN}
 368 and found no significant correlation. We chose $t_{BN} = 0.5$ h and $\Delta T_{BN} = 2$ h.

5. Solar wind driven model for electron plasma sheet densities and temperatures: Empirical relations

369 Using the time constants given in Table 5, we computed the input parameters for the
 370 electron density and temperature models as time integrals in the form of Equation 2.
 371 Note that the lag values in Table 5 (0.58 h) are different from those determined in Sec-
 372 tions 4.2 and 4.3 (0.5 h). The lag constants in Table 5 just take into account 5-min offset
 373 of the solar wind parameters used in this study (See Section 4.1).

374 At the first step, we use the following functional form of the plasma sheet parameter
 375 dependence on the solar wind input parameters:

$$376 \quad P_{ps} = G_0(\phi, R) + \sum_{j=1, \dots} G_j(\phi, R) \cdot P_j^{SW}, \quad (3)$$

377 where P_j^{SW} are the corresponding solar wind parameters, and $G_j(\phi, R)$ are the 2nd
 378 order polynomials of an azimuth angle ϕ and radial distance R given as

$$379 \quad G_j(\phi, R) = \sum_{m,n=0,1,2} C_{mnj} \cdot R^n \phi^m. \quad (4)$$

380 The polynomial coefficients C_{mnj} were found by fitting Equation 3 to the data (primary
 381 data set). After the first set of the coefficients was found, we computed the correlation
 382 coefficient between the plasma sheet parameters and the model predictions. Using this

383 correlation coefficient as a reference value, we started to remove more and more terms
 384 from Equation 3 (simplifying the polynomials) seeking for a minimal set of terms which
 385 still provide good model quality. That is, for every possible subset of the terms in Equa-
 386 tion 3, we fitted this truncated model to the data and computed the correlation coefficient
 387 between the data and the model. Comparing this correlation coefficient with a reference
 388 one, we checked that such simplification of Equation 3 did not lead to significant reduction
 389 of the model quality. After this simplification was done, we introduced the nonlinear pa-
 390 rameters (exponential powers of the driving parameters) and checked if this modification
 391 leads to significant improvement. The downhill simplex algorithm was used for finding a
 392 minimum of the error function [*Nelder and Mead*, 1965].

393 Applying this method to the plasma sheet electron density and temperature datasets,
 394 we come up with following solutions. The number density in the plasma sheet (N_{ps}) is
 395 given in cm^{-3} as follows:

$$396 \quad N_{ps} = A_1 + A_2 R^* + A_3 \phi^{*2} R^* + A_4 \phi^{*2} + A_5 N_{sw}^* + (A_6 + A_7 R^*) B_S^*, \quad (5)$$

397 where, $\phi^* = \phi/90^\circ$, $R^* = R/10R_E$ are normalized coordinates, and N_{sw}^* , B_S^* are the
 398 time-integrated and normalized parameters characterizing the external conditions and
 399 defined as:

$$400 \quad N_{sw}^*(t_0) = \frac{1}{10 \text{ cm}^{-3} \Delta T_N} \int_{t_0 - t_N - \Delta T_N}^{t_0 - t_N} N_{sw}(t) dt, \quad (6)$$

$$401 \quad B_S^*(t_0) = \frac{1}{2 \text{ nT} \Delta T_{BS}} \int_{t_0 - t_{BS} - \Delta T_{BS}}^{t_0 - t_{BS}} B_S(t) dt. \quad (7)$$

Here, N_{sw} and B_S are the solar wind density and southward IMF component. The values for t_N , ΔT_N , t_{BS} and ΔT_{BS} are given in Table 5 and the model coefficients A_i are given in Table 6. Figure 8a shows the electron density values observed by THEMIS probes versus the model predictions.

The temperature in the plasma sheet (T_{ps}) is given in keV as follows:

$$T_{ps} = [A_1 + A_2\phi^* + A_3V_{sw}^* + (A_4 + A_5\phi^{*2}R^*)B_S^{*A_7} + A_6R^*B_N^{*A_8}]^{A_9}, \quad (8)$$

where

$$V_{sw}^*(t_0) = \frac{1}{400 \text{ km/s } \Delta T_V} \int_{t_0-t_V-\Delta T_V}^{t_0-t_V} V(t)dt, \quad (9)$$

$$B_S^*(t_0) = \frac{1}{2 \text{ nT } \Delta T_{BS}} \int_{t_0-t_{BS}-\Delta T_{BS}}^{t_0-t_{BS}} B_S(t)dt, \quad (10)$$

$$B_N^*(t_0) = \frac{1}{2 \text{ nT } \Delta T_{BN}} \int_{t_0-t_{BN}-\Delta T_{BN}}^{t_0-t_{BN}} B_N(t)dt. \quad (11)$$

Here, V_{sw} , B_S , and B_N are the solar wind density and the southward and northward IMF components, respectively. The values for t_V , ΔT_V , t_{BS} , ΔT_{BS} , t_{BN} and ΔT_{BN} are given in Table 5 and the model coefficients A_i are given in Table 6. Figure 9a shows the electron temperature values observed by THEMIS probes versus the model predictions. It can be seen that for high electron temperatures, the THEMIS measurements typically exceed the model prediction. This bias would be much stronger if the standard least-squared error function is used. In order to minimize the bias, we have modified the error function as follows:

D R A F T

August 18, 2016, 1:10am

D R A F T

$$ERR = \sum_j W \cdot |T_j^{THM} - T_j^{model}| \quad (12)$$

Here, T_j^{THM} and T_j^{model} are the THEMIS measurements and model predictions, respectively, and weight coefficient W is a linear function of T_j^{THM} changing from 1 at $T_j^{THM} = 0$ to 1.5 at $T_j^{THM} = 22$ keV.

6. Solar wind driven model for electron plasma sheet densities and temperatures: Results

Some properties of the empirical electron plasma models becomes evident after inspection of Equations 5 and 8 and Table 6. The resulting density model is very simple. Only terms symmetric with respect to the midnight meridian remain after the model simplification as described in Section 5. The symmetry of the density distribution is an interesting finding since the storm time inner magnetosphere is highly asymmetric (at least during the main phase). The plasma sheet density response to changes of the solar wind density is positive and uniform across whole region of the model applicability. It is a bit surprising, but the plasma sheet electron density response to the southward IMF component is also positive. *Tsyganenko and Mukai* [2003] reported opposite dependence. However, it should be noted that the model is parameterized by B_S lagged by 0.5 h and averaged over six hours, that is, this density response is not related to the substorm cycle but rather to the geomagnetic storm time-scale. In addition, this response is strongest in the near-Earth region and disappears at $r = 11R_E$, where *Tsyganenko and Mukai* [2003] model's validity region begins. This IMF B_S effect can be interpreted as a result of the compression of the flux tube due to inflation of the inner magnetosphere magnetic configuration caused by the ring current strengthening. However, we can not be sure that this effect manifests

440 only during storm-times. Figures 10a and 10b show the distribution of the plasma density
 441 in the equatorial plane. The corresponding input parameters are given at the top of each
 442 panel. The density increases towards the Earth and peaks at midnight. Note that the
 443 model reveals opposite MLT dependence at the outer boundary of the region (the density
 444 is highest near the dusk and dawn meridians). This feature manifests more clearly in
 445 Figure 10a and it is in agreement with *Tsyganenko and Mukai* [2003] model (see their
 446 Figure 10).

447 Figures 10c-f show the equatorial maps of the electron temperature distributions for four
 448 combinations of the model input parameters. In contrast to the density distributions, the
 449 electron temperature exhibits very strong dusk-dawn asymmetry. Figure 10c shows the
 450 temperature distribution for $B_S^* = B_N^* = 0$. In fact, it is unlikely that such combination
 451 of the parameters occur in reality since it implies that transverse component of IMF is
 452 zero for at least 45 minutes (see Table 5). For these parameters, the model temperature
 453 increases monotonically from dusk to dawn meridian showing no dependence on radial
 454 distance.

455 As it follows from Equation 8 and Table 6, the near-Earth plasma sheet electron temper-
 456 ature increases with the solar wind velocity increase. Although there is only one coefficient
 457 associated with V_{SW}^* in Equation 8, the electron temperature response to V_{SW}^* increase
 458 is not uniform since the left part of Equation 8 is raised to the power of 2.3 ($A_9 = 2.3$
 459 see Table 6). It means that the response is stronger on the dawn side where the electron
 460 temperature is higher.

461 The electron temperature increases with the southward IMF component increase. This
 462 effect is strongest near the midnight and disappears at the dawn and dusk MLTs. It

463 leads to the temperature peak localization in the midnight – dawn sector (See Fig-
464 ures 10d and 10f). The increase of IMF B_S leads to a shift of the temperature maximum
465 from the dawn sector towards midnight. The post-midnight location of the electron tem-
466 perature peak is probably related to the substorm activity (hot electrons drift eastward
467 from an injection place in pre-midnight sector).

468 The electron temperature response to the northward IMF component (integrated over
469 2 hours) is negative and strongest at the outer border of the region. Figure 10e demon-
470 strates the cooling of the electrons in the outer part of the region during the prolonged
471 periods of northward IMF. It is probably related to the arrival of the cold magnetosheath
472 plasma during the intervals of the northward IMF [*Wing et al.*, 2005; *Wang et al.*,
473 2007, 2010].

7. Discussion of the Model Performance

474 Figures 8a and 9a present the scatter plots of the model predictions versus real THEMIS
475 observations (primary data set) for electron density and temperature models, respectively.
476 The correlation coefficients between the model and the data were 0.82 for electron den-
477 sity and 0.75 for electron temperature models. Table 7 shows the correlation coefficients
478 between the model predictions and the real data (primary data set) computed for ev-
479 ery spatial bin separately. The root-mean-square deviations (RMS) and mean absolute
480 deviations (MAD) are also shown. It can be seen that both models show their best per-
481 formance on the dawnside of the region. It is not immediately clear what causes such
482 asymmetry. Since the electrons undergo eastward magnetic drifts, their drift trajectories
483 are expected to be regular on the dawnside, in contrast to the duskside where the drift
484 paths can bifurcate (especially in the near-Earth region). Substorm activity is typically

485 peaked at the pre-midnight sector (and this distortion can become even stronger during
486 the storm periods) and it can also contribute to the poorer performance of the model on
487 the duskside.

488 However, a model performance estimation using the same data the models has been fit-
489 ted to cannot be considered as an independent test. The auxiliary data set (see Section 3)
490 has not been used for the model coefficients determination. Indeed, it can be considered
491 as an almost independent data set because only 26% of its data have the "neighbours"
492 from primary data set within ± 30 min (these neighbours are typically measurements on
493 other probes). In addition, 20% of the auxiliary data set are referred to the early period
494 of the THEMIS mission (2007–2009) which is not included in the primary data set. This
495 theoretically allows us to check if there is any bias in the primary data set related to the
496 detectors degradation. On the other hand, the auxiliary data set represents unaveraged
497 ~ 3 -sec resolution measurements and we expect more noise in this data set and, hence,
498 poorer correlations. Finally, the auxiliary data set is three times smaller than the primary
499 data set and we can not expect that the model coefficients obtained by fitting the model
500 to the smaller data set are of the same accuracy level.

501 Table 8 shows the correlation coefficients and the average deviations between the model
502 and the auxiliary data set. Although the correlation coefficients are lower than those for
503 the primary data set, they are still higher than 0.7 (typical correlation for the empirical
504 models of the near-Earth plasma environment [*Tsyganenko and Mukai, 2003; Sergeev et*
505 *al., 2015*]). Strangely enough, the density model shows better agreement with auxiliary
506 data set on the dusk side but it might be an effect of limited statistics. The scatter
507 plots of the model prediction versus the data from auxiliary data set are presented in

508 Figures 8b and 9b. It can be seen that during high density periods, the models tend to
509 underestimate the density values for significant number of events. Although this feature
510 can be also noticed in Figures 8a for the primary data set, it is much more prominent in
511 Figure 8b. To rule out possibility that this difference between two data sets is due to the
512 detectors degradation, we inspected the data corresponding to these problematic points.
513 It turned out that only 11% of these data are referred to the years 2007–2009, indicating
514 that there is another reason of this discrepancy. We also checked the hypothesis that
515 this bias is caused by transient processes in the plasma sheet called bursty bulk flows
516 [Angelopoulos *et al.*, 1992; Baumjohann *et al.*, 1990]. However, the occurrence of events
517 with the ion flow velocity exceeding 100 km/s for the problematic points is similar to that
518 for the points near the diagonal of Figure 8b.

519 Finally, to test the model coefficient sensitivity to the change of the data set, we fitted
520 the model to the auxiliary data set. The resulting coefficients are presented in the bottom
521 part of Table 6. It can be seen that the difference between the density model coefficients
522 obtained by fitting to the different data set can be as large as factor 3 (see A_3 , A_4
523 coefficients). However, the difference between polynomials $A_1 + A_2R^* + A_3\phi^{*2}R^* + A_4\phi^{*2}$
524 (first four terms in Equation 5) is within 40%. The coefficients are not so different for the
525 temperature model.

526 Comparison of our models performance with other empirical models is not straightfor-
527 ward. On one hand, our electron density model shows the best correlations between the
528 model predictions and the data among all existing empirical models. On the other hand,
529 such an evaluation of the model performance is strongly biased. The regions of applica-
530 bility of our model and the models of other authors overlap only partly. The different

531 data sets were used for the construction of the models. Our data set includes storm-time
532 intervals. The solar wind driving parameters undergo stronger variations during storm
533 periods and all dependencies can be tracked more easily. On the other side, these highly
534 disturbed periods obviously add more scatter to the data.

535 The correlation of the *Tsyganenko and Mukai* [2003] ion temperature model predictions
536 with the data is comparable with that for our model for electron temperature (0.71 versus
537 0.75, respectively). The comparison of the ion and electron models seems to be justified
538 because the ion and electron temperatures are highly correlated in the central plasma sheet
539 [*Baumjohann et al.*, 1989]. It should be mentioned that the correlations in the *Tsyganenko*
540 *and Mukai* [2003] study were computed for the whole region of the models applicability.
541 Since the *Tsyganenko and Mukai* [2003] model covers the magnetotail between $r = 10$ –
542 $50R_E$, and the ion temperature reveals a stable increase with distance, a simple comparison
543 of the correlations for the whole data sets puts the *Tsyganenko and Mukai* [2003] model in
544 the more favorable conditions. On the other hand, the highly dynamic bursty bulk flows
545 occur more frequently in the distant plasma sheet [*Baumjohann et al.*, 1990]. In addition,
546 *Runov et al.* [2015] found that the correlation between the ion and electron temperatures
547 disappears at $r < 12R_E$ and *Artemyev et al.* [2011] found that the relation between the
548 electron and ion temperatures is non-linear in the mid-tail.

549 For development in the future, we foresee the following possibilities: (1) A presence of
550 the multiple population components (cold, hot) should be addressed; (2) The inclusion
551 of the geomagnetic activity indices as input parameters will increase the model accuracy;
552 (3) Expansion of the dataset including non-storm periods.

8. Conclusions

553 The empirical models of the plasma sheet electron temperature and density on the
554 nightside for $6R_E < r < 11R_E$ has been constructed using the data of the THEMIS
555 mission obtained during the geomagnetic storm periods. The models depend on spatial
556 coordinates as well as on the interplanetary medium parameters. The reader can find the
557 codes for both models as well as procedures for the input parameters computation in the
558 supplemental materials.

559 The model performances have been essentially improved by using lagged and time aver-
560 aged solar wind parameters as model inputs. The best time-lag and duration of averaging
561 were different for different parameters as well as showed some dependence on MLT (the
562 latter feature is not included in the current model version).

563 It was found that the plasma sheet electron density equatorial distribution is symmet-
564 ric with respect to the midnight meridian. It reveals a strong earthward gradient and a
565 moderate symmetric variation with MLT. The plasma sheet density dependence on the
566 external driving is parameterized by the solar wind proton density (averaged over pre-
567 ceding 4 hours) and southward IMF component (averaged over preceding 6 hours). In
568 agreement with results of previous studies, the solar wind proton density is the main
569 controlling parameter but the IMF B_S becomes of almost the same importance in the
570 near-Earth region. The model density shows a positive response to the increase of either
571 input parameter. The electron density revealed better correlation with IMF B_S averaged
572 over the time interval which is closer to the geomagnetic storm main phase (~ 6 hours)
573 rather than the substorm growth phase (~ 45 minutes). The root-mean-square deviation
574 between the observed and predicted plasma sheet density values is 0.23 cm^{-3} and the

575 correlation coefficient is 0.82, the highest correlation with the data set ever obtained for
576 these kinds of empirical models.

577 The electron temperature model is highly asymmetric with respect to the local midnight.
578 The electron temperature maximum is located in the post-midnight – morning MLT
579 sector. The model is parameterized by solar wind velocity and southward and northward
580 components of IMF. The solar wind velocity is a major controlling parameter and the
581 importance of B_S and B_N is comparable. The plasma sheet electron temperature responds
582 positively to the solar wind velocity and IMF B_S increase and it responds negatively to the
583 IMF B_N increase. In contrast to the density model, the electron temperature shows higher
584 correlation with the southward IMF component when IMF B_S is averaged over preceding
585 ~ 45 min (substorm growth phase time scale). The effect of the northward component is
586 parameterized by ~ 2 hour average of IMF B_N . The impact of the prolonged IMF B_N
587 manifests mostly in the outer part of the modelled region ($r > 8R_E$) while the influence
588 of the IMF B_S is maximal in the midnight – post-midnight MLT sector. The correlation
589 coefficient between the observed and predicted plasma sheet electron temperature values
590 is 0.76 and the root-mean-square deviation is 2.6 keV.

591 The both models reveal the dawn-dusk asymmetry of their performances with better
592 accuracy achieved in the dawn MLT sector. The correlations between the model predic-
593 tions and observations vary between C.C. >0.7 in the dawn MLT sector and C.C.= 0.5–0.7
594 in the dusk sector.

595 Acknowledgments.

596 The plasma moments were obtained from the THEMIS mission web site
597 (<http://themis.ssl.berkeley.edu/index.shtml>). The solar wind and IMF data were

598 downloaded from the OMNI database from the GSFC/SPDF OMNIWeb interface at
599 <http://omniweb.gsfc.nasa.gov>. The 1-min. resolution SYM-H index was provided by the
600 World Data Center for geomagnetism, Kyoto (<http://wdc.kugi.kyoto-u.ac.jp/>). The part
601 of the research done by N. Ganushkina and S. Dubyagin has received funding from the
602 European Union Seventh Framework Programme (FP7/20072013) under grant agreement
603 606716 SPACESTORM and from the European Union Horizon 2020 Research and Inno-
604 vation programme under grant agreement 637302 PROGRESS. N. Ganushkina thanks the
605 International Space Science Institute in Bern, Switzerland, for their support of the interna-
606 tional teams on “Analysis of Cluster Inner Magnetosphere Campaign data, in application
607 the dynamics of waves and wave-particle interaction within the outer radiation belt” and
608 “Ring current modeling: Uncommon Assumptions and Common Misconceptions”.

References

- 609 Artemyev, A. V., Baumjohann, W., Petrukovich, A. A., Nakamura, R., Dandouras, I., and
610 Fazakerley, A.: Proton/electron temperature ratio in the magnetotail, *Ann. Geophys.*,
611 *29*, 2253–2257, doi:10.5194/angeo-29-2253-2011, 2011.
- 612 Artemyev, A. V., Petrukovich, A. A., Nakamura, R., and Zelenyi, L. M. (2013), Profiles of
613 electron temperature and Bz along Earth’s magnetotail, *Ann. Geophys.*, *31*, 1109–1114,
614 doi:10.5194/angeo-31-1109-2013.
- 615 Auster, H. U., et al. (2008), The THEMIS fluxgate magnetometer, *Space Sci. Rev.*, *141*,
616 235–236, doi: 10.1007/s11214-008-9365-9.
- 617 Angelopoulos, V., W. Baumjohann, C. F. Kennel, F. V. Coroniti, M. G. Kivelson, R.
618 Pellat, R. J. Walker, H. Lühr, and G. Paschmann (1992), Bursty bulk flows in the inner

- 619 central plasma sheet, *J. Geophys. Res.*, *97(A4)*, 4027-4039, doi:10.1029/91JA02701.
- 620 Angelopoulos, V. (2008a), The THEMIS mission, *Space Sci. Rev.*, *141*, 5–34,
621 doi:10.1007/s11214-008-9336-1.
- 622 Angelopoulos, V, D. Sibeck, C.W. Carlson, et al. (2008b), First Results from the THEMIS
623 mission, *Space Sci. Rev.*, *141*, 453–476.
- 624 Baumjohann, W., G. Paschmann, and C. A. Cattell (1989), Average plasma
625 properties in the central plasma sheet, *J. Geophys. Res.*, *94(A6)*, 6597-6606,
626 doi:10.1029/JA094iA06p06597.
- 627 Baumjohann, W., G. Paschmann, and H. Lühr (1990), Characteristics of high-
628 speed ion flows in the plasma sheet, *J. Geophys. Res.*, *95(A4)*, 3801-3809,
629 doi:10.1029/JA095iA04p03801.
- 630 Borovsky, J. E., M. F. Thomsen, and R. C. Elphic (1998a), The driving of the plasma sheet
631 by the solar wind, *J. Geophys. Res.*, *103(A8)*, 17617-17639, doi:10.1029/97JA02986.
- 632 Borovsky, J. E., M. F. Thomsen, R. C. Elphic, T. E. Cayton, and D. J. McComas (1998b),
633 The transport of plasma sheet material from the distant tail to geosynchronous orbit,
634 *J. Geophys. Res.*, *103(A9)*, 20297-20331, doi:10.1029/97JA03144.
- 635 Burin des Rozières, E., X. Li, D.N. Baker, T.A. Fritz, R. Friedel, T.G. Onsager, and
636 I. Dandouras (2009), Energetic plasma sheet electrons and their relationship with
637 the solar wind: A cluster and geotail study, *J. Geophys. Res.*, *114*, A02220, DOI:
638 10.1029/2008JA013696.
- 639 Chen Y., R. H. W. Friedel, G. D. Reeves, PSD distributions of energetic elec-
640 trons in the outer radiation belt during two Geospace Environment Modeling
641 Inner Magnetosphere/Storms selected storms, *J. Geophys. Res.*, *111*, A11S04,

642 doi:10.1029/2006JA011703, 2006.

643 Davis, V. A., M. J. Mandell, and M. F. Thomsen (2008), Representation of the measured
644 geosynchronous plasma environment in spacecraft charging calculations, *J. Geophys.*
645 *Res.*, *113*, A10204, doi:10.1029/2008JA013116.

646 Denton, M. H., M. F. Thomsen, H. Korth, S. Lynch, J. C. Zhang, and M. W. Liemohn
647 (2005), Bulk plasma properties at geosynchronous orbit, *J. Geophys. Res.*, *110*, A07223,
648 doi:10.1029/2004JA010861.

649 Denton, M. H., M. F. Thomsen, V. K. Jordanova, M. G. Henderson, J. E. Borovsky,
650 J. S. Denton, D. Pitchford, and D. P. Hartley (2015), An empirical model of electron
651 and ion fluxes derived from observations at geosynchronous orbit, *Space Weather*, *13*,
652 doi:10.1002/2015SW001168.

653 Dubyagin, S., V. Sergeev, S. Apatenkov, V. Angelopoulos, R. Nakamura, J. McFad-
654 den, D. Larson, and J. Bonnell (2010), Pressure and entropy changes in the flow-
655 braking region during magnetic field dipolarization, *J. Geophys. Res.*, *115*, A10225,
656 doi:10.1029/2010JA015625.

657 Friedel, R. H. W., H. Korth, M. G. Henderson, M. E. Thomsen, J. D. Scudder (2001),
658 Plasma sheet access to the inner magnetosphere, *J. Geophys. Res.*, *106*, 5845-5858.

659 Jordanova, V. K., and Y. S. Miyoshi (2005), Relativistic model of ring current and
660 radiation belt ions and electrons: Initial results, *Geophys. Res. Lett.*, *32*, L14104,
661 doi:10.1029/2005GL023020.

662 Jordanova, V. K., Y. Yu, J. T. Niehof, R. M. Skoug, G. D. Reeves, C. A. Kletzing, J. F.
663 Fennell, and H. E. Spence (2014), Simulations of inner magnetosphere dynamics with
664 an expanded RAM-SCB model and comparisons with Van Allen Probes observations,

- 665 *Geophys. Res. Lett.*, *41*, 2687-2694, doi:10.1002/2014GL059533.
- 666 Ganushkina N. Yu., O. Amariutei, Y. Y. Shpritz, and M. Liemohn (2013), Transport
667 of the plasma sheet electrons to the geostationary distances, *J. Geophys. Res.*, *118*,
668 doi:10.1029/2012JA017923.
- 669 Ganushkina N. Yu., M. Liemohn, O. Amariutei, and D. Pitchford (2013b), Low en-
670 ergy electrons (5-50 keV) in the inner magnetosphere, *J. Geophys. Res.*, *119*, 246259,
671 doi:10.1002/2013JA019304.
- 672 Ganushkina, N. Y., O. A. Amariutei, D. Welling, and D. Heynderickx, (2015), Nowcast
673 model for low-energy electrons in the inner magnetosphere, *Space Weather*, *13*, 1634,
674 doi:10.1002/2014SW001098.
- 675 Garrett, H. B. (1981), The charging of spacecraft surfaces, *Rev. Geophys.*, *19*(4), 577,
676 doi:10.1029/RG019i004p00577.
- 677 Kaufmann, R. L., W. R. Paterson, and L. A. Frank (2005), Relationships between the
678 ion flow speed, magnetic flux transport rate, and other plasma sheet parameters, *J.*
679 *Geophys. Res.*, *110*, A09216, doi:10.1029/2005JA011068.
- 680 Kerns, K. J., D. A. Hardy, and M. S. Gussenhoven, Modeling of convection boundaries
681 seen by CRRES in 120-eV to 28-keV particles, *J. Geophys. Res.*, *99*, 2403, 1994.
- 682 Korth, H., M. F. Thomsen, J. E. Borovsky, and D. J. McComas (1999), Plasma sheet
683 access to geosynchronous orbit, *J. Geophys. Res.*, *104*, 25,047-25,061.
- 684 Kurita, S., Y. Miyoshi, F. Tsuchiya, Y. Nishimura, T. Hori, Y. Miyashita, T. Takada, A.
685 Morioka, V. Angelopoulos, J. P. McFadden, H. U. Auster, J. M. Albert, V. Jordanova,
686 and H. Miyawa et al. (2011), Transport and loss of the inner plasma sheet electrons:
687 THEMIS observations, *J. Geophys. Res.*, *116*, A03201, doi:10.1029/2010JA015975.

- 688 Lanzerotti, L. J., K. LaFleur, C. G. Maclellan, and D. W. Maurer (1998), Geosyn-
689 chronous spacecraft charging in January 1997, *Geophys. Res. Lett.*, *25*(15), 2967-2970.
- 690 Liemohn, M. W., G. V. Khazanov, and J. U. Kozyra (1998), Banded electron structure
691 formation in the inner magnetosphere, *Geophys. Res. Lett.*, *25*, 877.
- 692 Mauk, B. H., and C.-I. Meng (1983), Characterization of geostationary particle signatures
693 based on the "Injection Boundary" model, *J. Geophys. Res.*, *88*, 3055.
- 694 McFadden, J. P., Carlson, C. W., Larson, D., Angelopoulos, V., Ludlam, M., Abiad, R.,
695 Elliott, B., Turin, P., Marckwordt, M. (2008), The THEMIS ESA plasma instrument
696 and in-flight calibration, *Space Sci. Rev.*, *141*, 277–302, doi: 10.1107/s11214-008-9440-2
- 697 McFadden, J.P., Carlson, C.W., Larson, D., Bonnell, J., Mozer, F., Angelopoulos, V.,
698 Glassmeier, K.-H., Auster, U. (2008), THEMIS ESA first science results and perfor-
699 mance issues. *Space Sci. Rev.*, *141*, 477–508, doi:10.1007/s11214-008-9433-1.
- 700 Miyoshi, Y. S., V. K. Jordanova, A. Morioka, M. F. Thomsen, G. D. Reeves, D. S. Evans,
701 and J. Green (2006), Observations and modeling of energetic electron dynamics dur-
702 ing the October 2001 storm, *J. Geophys. Res.*, *111*, A11S02, doi:10.1029/2005JA011351.
- 703 Nelder, John A.; R. Mead (1965), A simplex method for function minimization, *Computer*
704 *Journal*, *7*, 308-313, doi:10.1093/comjnl/7.4.308
- 705 Runov, A., V. Angelopoulos, C. Gabrielse, J. Liu, D. L. Turner, and X.-Z.
706 Zhou (2015), Average thermodynamic and spectral properties of plasma in and
707 around dipolarizing flux bundles. *J. Geophys. Res. Space Physics*, *120*, 4369-4383,
708 doi:10.1002/2015JA021166.
- 709 Sergeev, V. I., N. P. Dmitrieva, N. A. Stepanov, D. A. Sormakov, V. Angelopoulos, and
710 A. V. Runov (2015), On the plasma sheet dependence on solar wind and substorms

711 and its role in magnetosphere-ionosphere coupling. *Earth, Planets and Space*, *67*, doi:
712 10.1186/s40623-015-0296-x.

713 Shukhtina, M. A., N. P. Dmitrieva, N. G. Popova, V. A. Sergeev, A. G. Yahnin, and I. V.
714 Despirak (2005), Observational evidence of the loading-unloading substorm scheme,
715 *Geophys. Res. Lett.*, *32*, L17107, doi:10.1029/2005GL023779.

716 Sicard-Piet, A., S. Bourdarie, D. Boscher, R. H. W. Friedel, M. Thomsen, T.
717 Goka, H. Matsumoto, and H. Koshiishi (2008), A new international geostationary
718 electron model: IGE-2006, from 1 keV to 5.2 MeV, *Space Weather*, *6*, S07003,
719 doi:10.1029/2007SW000368.

720 Terasawa, T., M. Fujimoto, T. Mukai, I. Shinohara, Y. Saito, T. Yamamoto, S. Machida,
721 S. Kokubun, A. J. Lazarus, J. T. Steinberg, and R. P. Lepping (1997), Solar wind
722 control of density and temperature in the near-Earth plasma sheet: WIND/GEOTAIL
723 collaboration. *Geophys. Res. Lett.*, *24*, 8, 935-938, doi: 10.1029/96GL04018.

724 Thomsen, M. F., M. G. Henderson, and V. K. Jordanova (2013), Statistical properties of
725 the substorm charging environment at geosynchronous orbit, *Space Weather*, *11*, 237244,
726 doi:10.1002/swe.20049.

727 Tsyganenko, N. A., and T. Mukai (2003), Tail plasma sheet models derived from Geotail
728 particle data. *J. Geophys. Res.*, *108*, 1136, doi:10.1029/2002JA009707, A3.

729 Tsyganenko, N. A., and D. H. Fairfield (2004), Global shape of the magnetotail cur-
730 rent sheet as derived from Geotail and Polar data, *J. Geophys. Res.*, *109*, A03218,
731 doi:10.1029/2003JA010062.

732 Wang, C.-P., L. R. Lyons, J. M. Weygand, T. Nagai, and R. W. McEntire (2006), Equa-
733 torial distributions of the plasma sheet ions, their electric and magnetic drifts, and

- 734 magnetic fields under different interplanetary magnetic field B_z conditions, *J. Geophys.*
735 *Res.*, *111*, A04215, doi:10.1029/2005JA011545.
- 736 Wang, C.-P., L. R. Lyons, T. Nagai, J. M. Weygand, and R. W. McEntire (2007), Sources,
737 transport, and distributions of plasma sheet ions and electrons and dependences on
738 interplanetary parameters under northward interplanetary magnetic field, *J. Geophys.*
739 *Res.*, *112*, A10224, doi:10.1029/2007JA012522.
- 740 Wang, C.-P., L. R. Lyons, T. Nagai, J. M. Weygand, and A. T. Y. Lui (2010), Evolution of
741 plasma sheet particle content under different interplanetary magnetic field conditions,
742 *J. Geophys. Res.*, *115*, A06210, doi:10.1029/2009JA015028.
- 743 Wang, C.-P., M. Gkioulidou, L. R. Lyons, and V. Angelopoulos (2012), Spatial distribu-
744 tions of the ion to electron temperature ratio in the magnetosheath and plasma sheet,
745 *J. Geophys. Res.*, *117*, A08215, doi:10.1029/2012JA017658.
- 746 Wing, S., and P. T. Newell, 2D plasma sheet ion density and temperature profiles for
747 northward and southward IMF, *Geophys. Res. Lett.*, *29*(9), doi:10.1029/2001GL013950,
748 2002.
- 749 Wing, S., J. R. Johnson, P. T. Newell, and C.-I. Meng (2005), Dawn-dusk asymmetries,
750 ion spectra, and sources in the northward interplanetary magnetic field plasma sheet,
751 *J. Geophys. Res.*, *110*, A08205, doi:10.1029/2005JA011086.
- 752 Åsnes, A., R. W. H. Friedel, B. Lavraud, G. D. Reeves, M. G. G. T. Taylor, and P. Daly
753 (2008), Statistical properties of tail plasma sheet electrons above 40 keV, *J. Geophys.*
754 *Res.*, *113*, A03202, doi:10.1029/2007JA012502.

Figure 1. (a) Spatial coverage of the equatorial magnetosphere by THEMIS observations. Only every tenth point is shown. Color shows corresponding SYM-H. (b) Spatial bins numeration.

Figure 2. Sketch explaining how to interpret Figures 3–7. The horizontal axis represents the time lag and the vertical axis represents duration of averaging. See explanation in the text.

Author Manuscript

Figure 3. Correlation coefficients (color coded) between the plasma sheet electron density and the solar wind density for six regions of the magnetotail. Vertical and horizontal axes show the solar wind density average duration and the lag of the solar wind density observations with respect to plasma sheet measurements. The oblique lines show $\Delta T_N = \text{const} - 2 \cdot t_N$ dependencies. The black filled circles mark ΔT_N and t_N which are used for the input parameters computation.

D R A F T

August 18, 2016, 1:10am

D R A F T

Author Manuscript

Figure 4 The same as Figure 3 but for correlation coefficients between the plasma sheet electron density and the southward component of IMF B_Z .

D R A F T

August 18, 2016, 1:10am

D R A F T

Author Manuscript

Figure 5 The same as Figure 3 but for correlation coefficients between the plasma sheet electron temperature and the solar wind velocity.

D R A F T

August 18, 2016, 1:10am

D R A F T

Author Manuscript

Figure 6 The same as Figure 3 but for correlation coefficients between the plasma sheet electron temperature and southward component of IMF B_Z .

D R A F T

August 18, 2016, 1:10am

D R A F T

Author Manuscript

Figure 7 The same as Figure 3 but for correlation coefficients between the plasma sheet electron temperature and the northward component of IMF B_Z .

D R A F T

August 18, 2016, 1:10am

D R A F T

Figure 8. Plasma sheet electron density predicted by the empirical model versus that measured by the THEMIS probes. (a) The THEMIS measurements are represented by primary data set. Every tenth point is shown. (b) The THEMIS measurements are represented by auxiliary data set. Every third point is shown.

Figure 9. The same as Figure 8 but for the electron temperature model.

Author Manuscript

Figure 10 Distributions of the electron temperature and density in the equatorial plane. (a–b) density model, (c–f) electron temperature model.

D R A F T

August 18, 2016, 1:10am

D R A F T

Table 1. Distribution of the number of the samples over the THEMIS mission period for primary and auxiliary data sets.

Years	2007	2008	2009	2010	2011	2012	2013
# primary	0	0	0	7475	11347	12693	13486
# auxiliary	1992	583	38	1688	2033	2520	3317

Table 2. Statistical properties of the data sets for different spatial bins. Top part is for standard deviations of instant values corresponding to the zero lag, and the bottom part shows the range of standard deviations found for lags between 0 and 12 h.

Bin index	1	2	3	4	5	6
$r, [A_E]$	8.5–11	8.5–11	8.5–11	6–8.5	6–8.5	6–8.5
ϕ	-90° – -30°	-30° – 30°	30° – 90°	-90° – -30°	-30° – 30°	30° – 90°
#	16257	9046	4698	6780	5812	2295
$\bar{n}N_{sw}, [\text{cm}^{-3}]$	5.1	3.7	5.1	6.0	4.3	3.5
$\sigma V_{sw}, \text{km/s}$	118	109	88	112	110	93
$\sigma B_{Z_{MF}}, \text{nT}$	4.0	3.9	4.0	4.4	3.9	3.6
$\sigma N_{SW}, [\text{cm}^{-3}]$	4.6-6.3	3.6-5.2	3.3-5.1	5.7-9.6	3.3-8.4	3.0-4.6
$\sigma V_{SW}, \text{km/s}$	117-121	106-111	88- 95	110-118	108-114	90- 98

Table 3. Correlations of the plasma sheet electron density with the solar wind parameters. Top part is for instant values $t_0 - 45$ min. and the bottom part shows best correlations found for all lags and durations of averaging.

Bin index	1	2	3	4	5	6
N_{SW}	0.71	0.54	0.60	0.69	0.57	0.39
IMF B_S	0.18	0.20	0.16	0.28	0.38	0.36
IMF B_N	0.24	0.33	0.35	0.16	0.13	0.08
N_{SW}	0.77	0.58	0.70	0.73	0.59	0.60
IMF B_S	0.33	0.35	0.42	0.58	0.48	0.47
IMF B_N	0.28	0.35	0.46	0.18	0.20	0.22

Table 4. Correlations of the plasma sheet electron temperature with the solar wind parameters.

Top part is for instant values $t_0 - 45$ min. and the bottom part shows best correlations found for all lags and durations of averaging.

Bin index	1	2	3	4	5	6
V_{SW}	0.59	0.63	0.28	0.59	0.59	0.31
IMF B_S	0.17	0.32	0.19	0.32	0.28	0.12
IMF B_N	-0.36	-0.29	-0.17	-0.42	-0.38	-0.23
V_{SW}	0.60	0.65	0.40	0.61	0.60	0.37
IMF B_S	0.19	0.34	0.26	0.36	0.30	0.25
IMF B_N	-0.42	-0.31	-0.25	-0.53	-0.39	-0.32

Table 5. Time constants for computation of the empirical models input parameters.

	t_N	ΔT_N	t_{BS}	ΔT_{BS}	t_V	ΔT_V	t_{BN}	ΔT_{BN}
Density	0.58 h	4.00 h	0.58 h	6.00 h				
Temperature			0.58 h	0.75 h	0.58 h	4.00 h	0.58 h	2.00 h

Table 6. Empirical model parameters.

	A_1	A_2	A_3	A_4	A_5	A_6	A_7	A_8	A_9
Density	1.23	-1.01	0.874	-0.820	0.392	0.521	-0.474		
Temperature	-0.0215	-0.426	1.47	0.587	-0.538	-0.489	0.32	0.36	2.31
Density [†]	1.01	-0.747	0.303	-0.248	0.362	0.498	-0.474		
Temperature [†]	-0.0922	-0.390	1.64	0.767	-1.02	-0.395	0.26	0.52	2.16

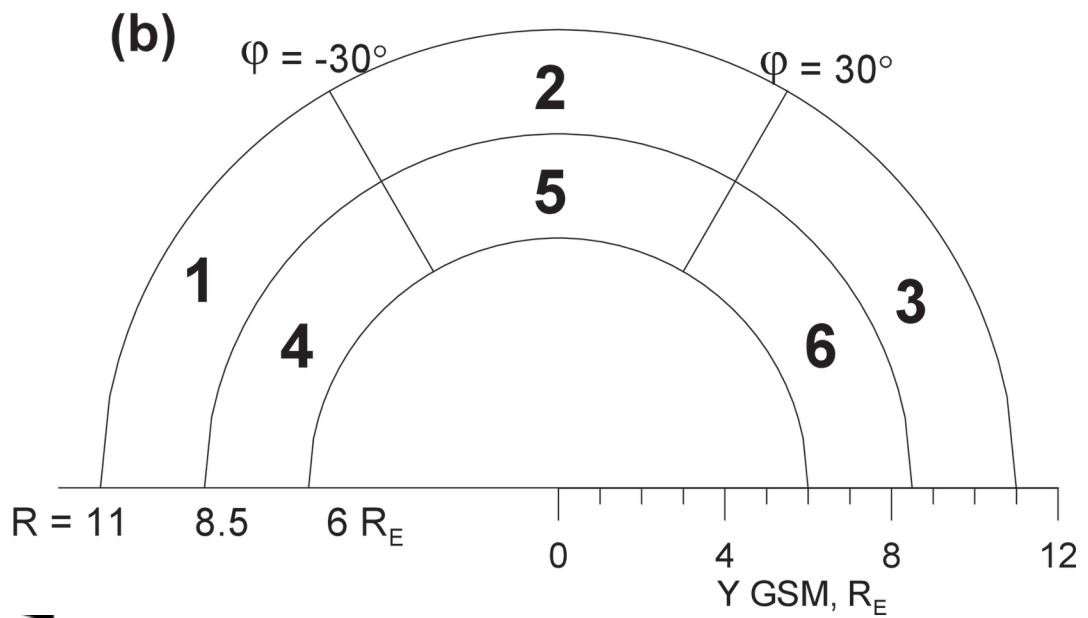
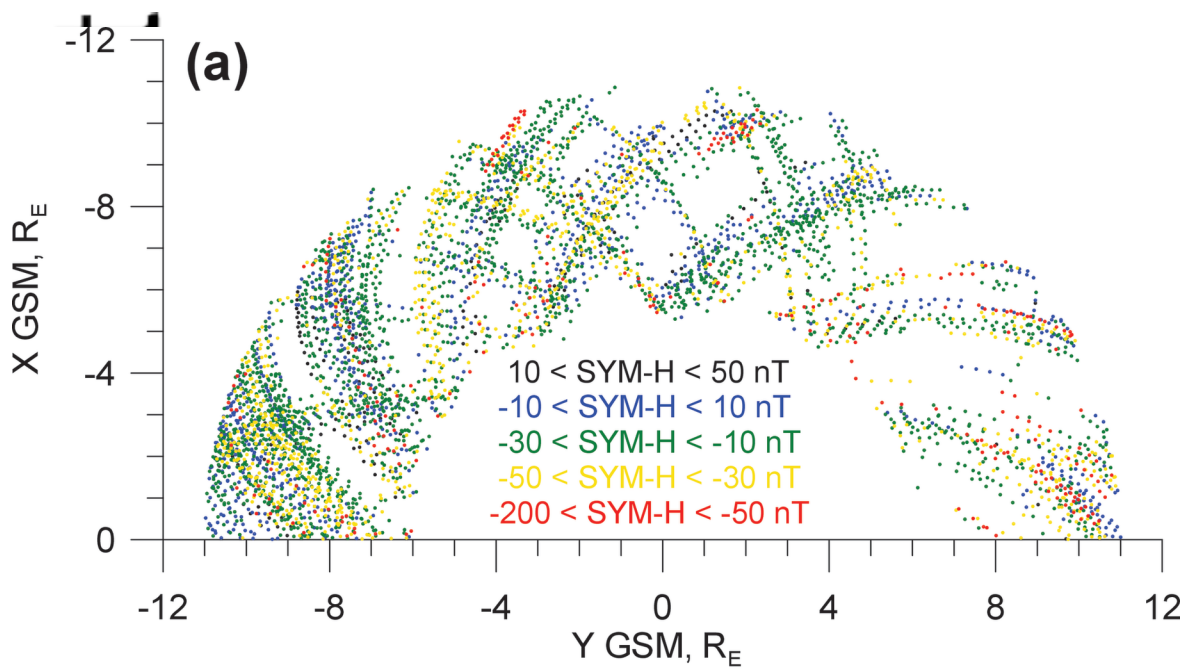
[†] Model coefficients obtained by fitting the model to the auxiliary data set.

Table 7. Characteristics of the empirical models quality. Top part of the table for the electron density model and the bottom one is for the temperature model

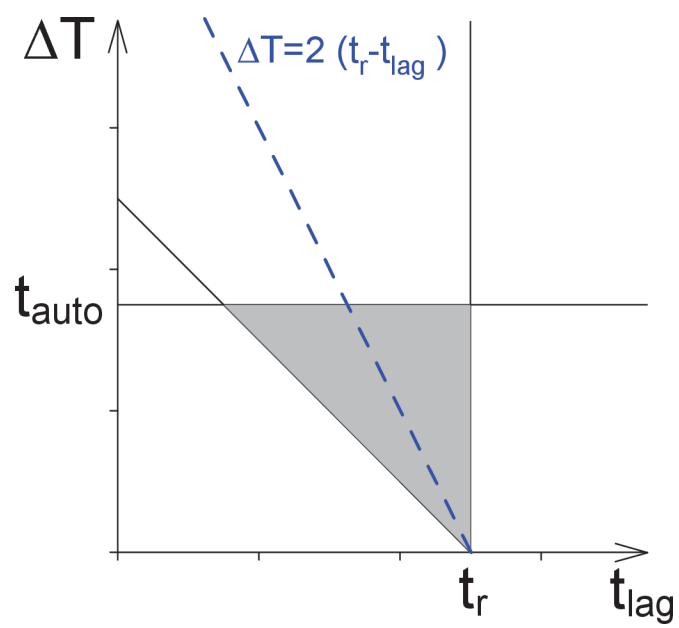
Bin index	all	1	2	3	4	5	6
C.C.	0.82	0.77	0.73	0.70	0.84	0.73	0.72
RMS, [cm^{-3}]	0.23	0.21	0.16	0.17	0.28	0.29	0.32
MAD, [cm^{-3}]	0.15	0.13	0.11	0.13	0.20	0.22	0.23
C.C.	0.75	0.72	0.72	0.65	0.79	0.75	0.54
RMS, [keV]	2.6	2.5	3.1	2.0	2.4	2.9	2.3
MAD, [keV]	1.8	1.8	2.1	1.3	1.8	2.1	1.7

Table 8. The same as Table 7 but for comparison with auxiliary data set. In addition, a number of data records for every bin is given in the second line.

Bin index	all	1	2	3	4	5	6
#	12171	5220	1211	1069	2922	1014	689
C.C.	0.73	0.61	0.70	0.70	0.63	0.79	0.80
RMS, [cm^{-3}]	0.28	0.27	0.18	0.19	0.34	0.32	0.28
MAD, [cm^{-3}]	0.19	0.16	0.12	0.14	0.25	0.23	0.21
C.C.	0.71	0.75	0.65	0.82	0.72	0.67	0.57
RMS, [keV]	3.1	2.4	3.6	3.7	2.9	4.3	4.2
MAD, [keV]	2.2	1.8	2.5	2.2	2.2	3.0	3.0

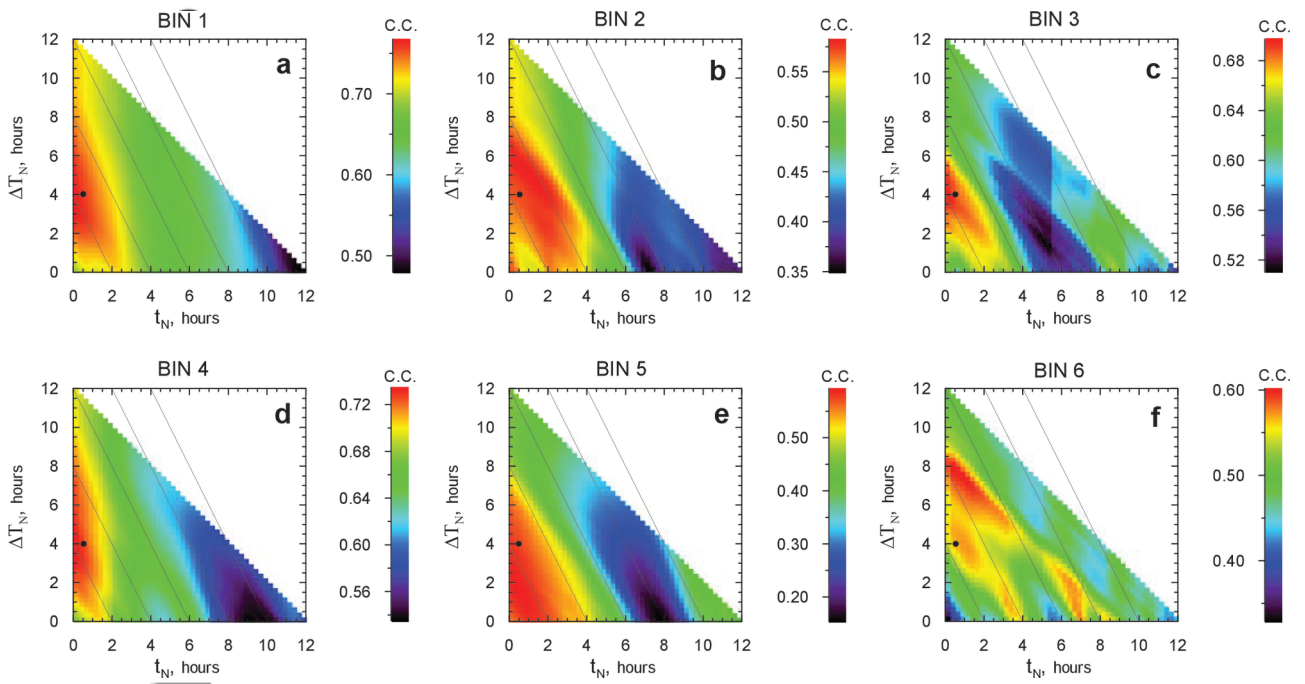


2016ja022947-f01-z-.eps



2016ja022947-f02-z-eps

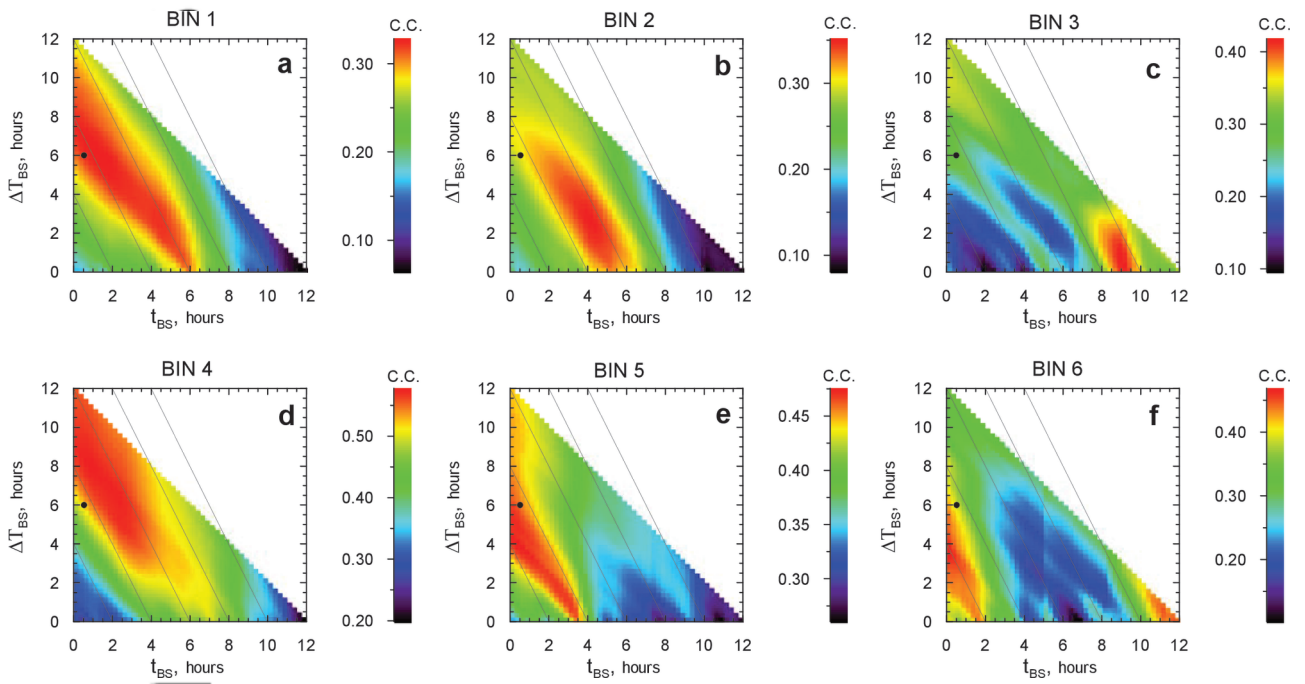
cript



2016ja022947-f03-z-eps

Auth

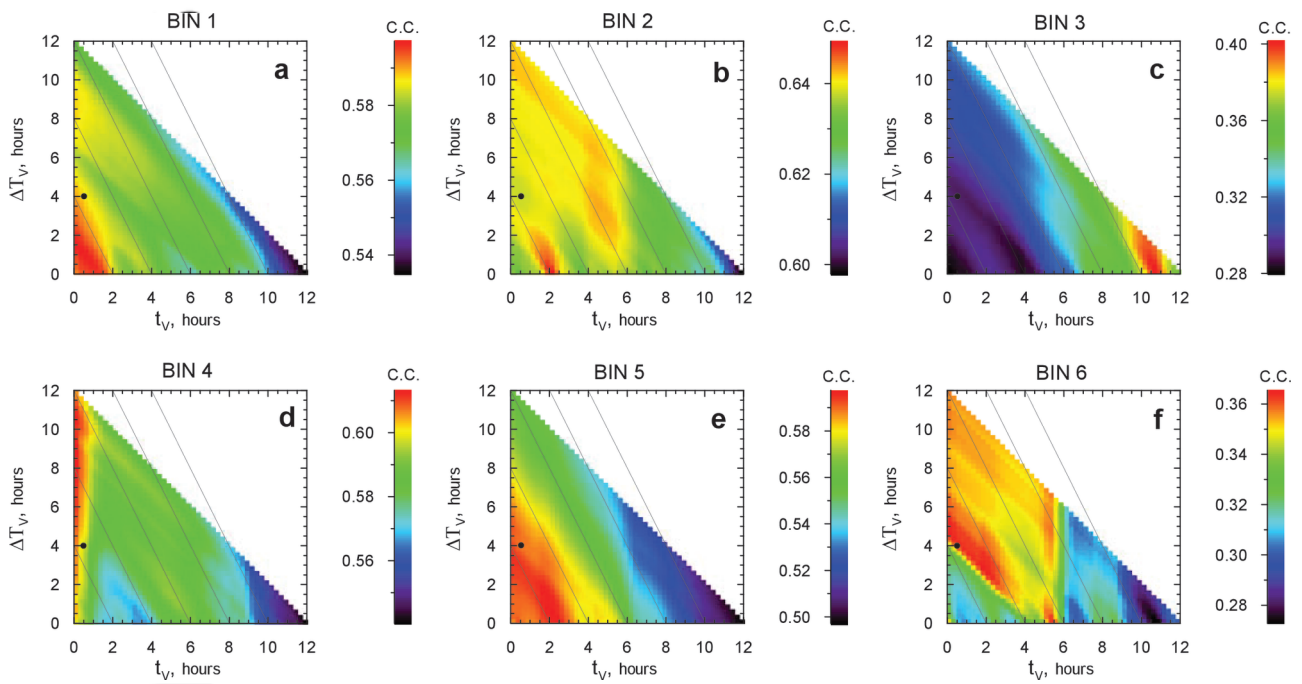
cript



2016ja022947-f04-z-eps

Auth

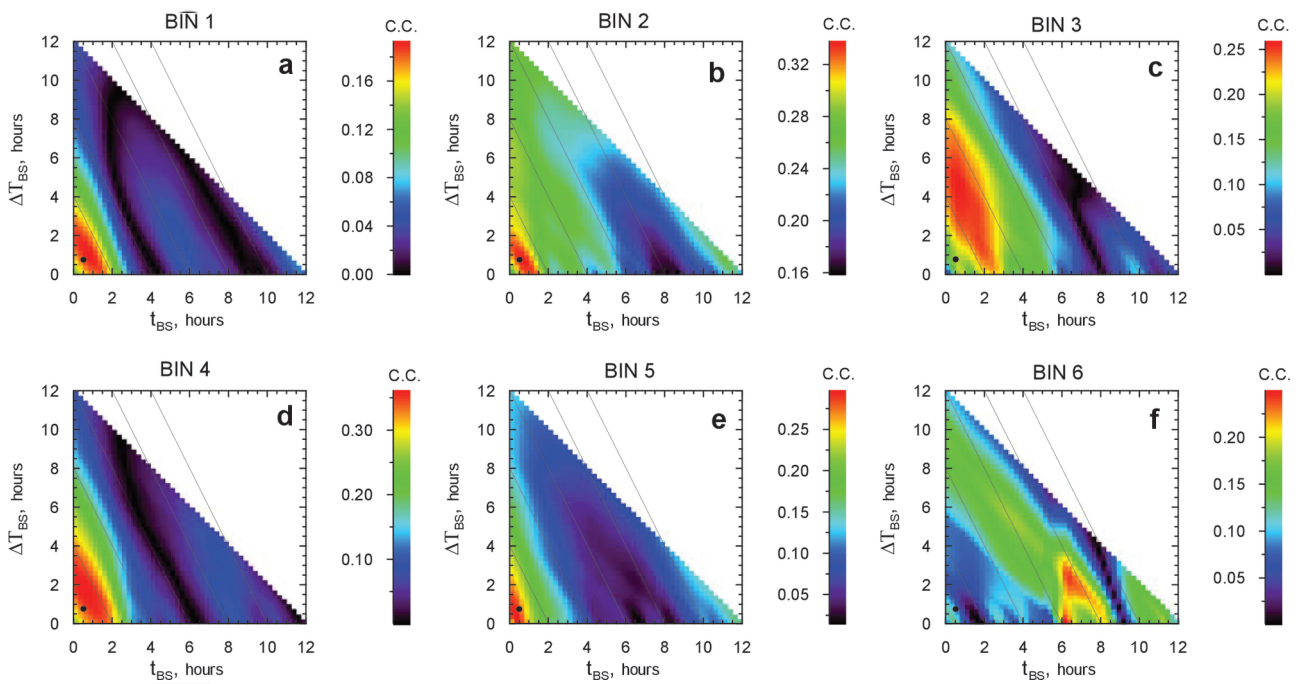
cript



2016ja022947-f05-z-.eps

Auth

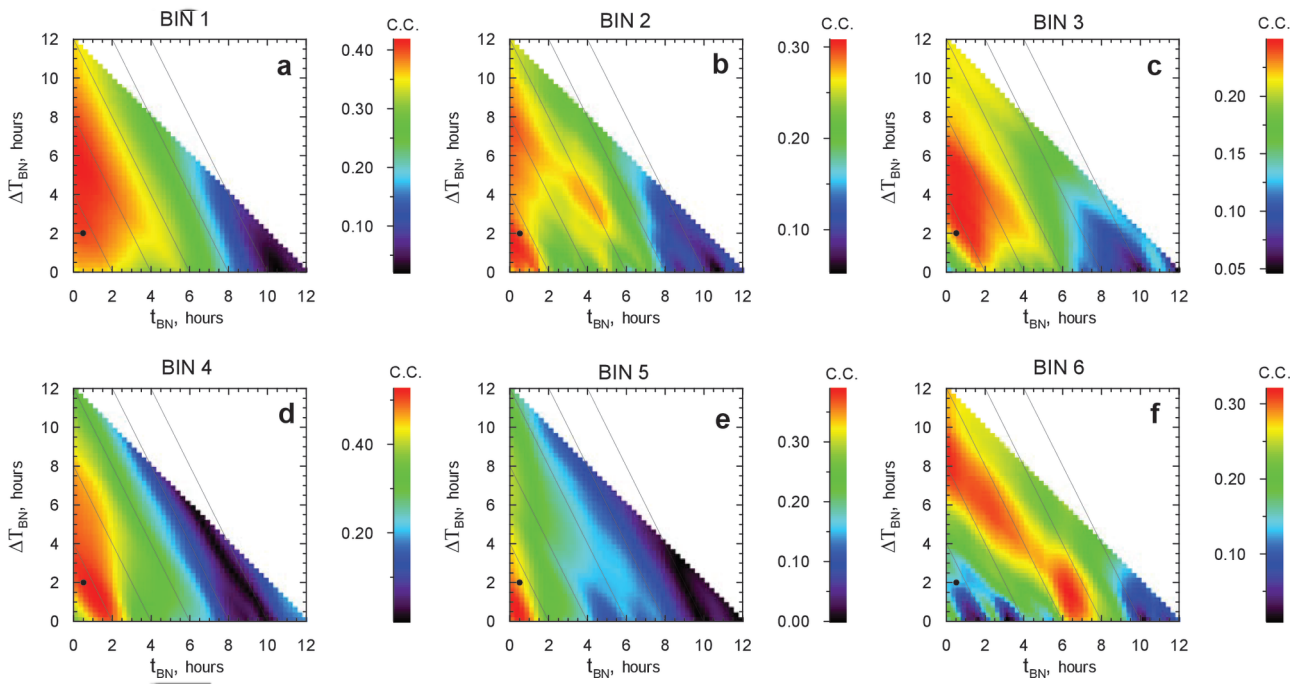
cript



2016ja022947-f06-z-.eps

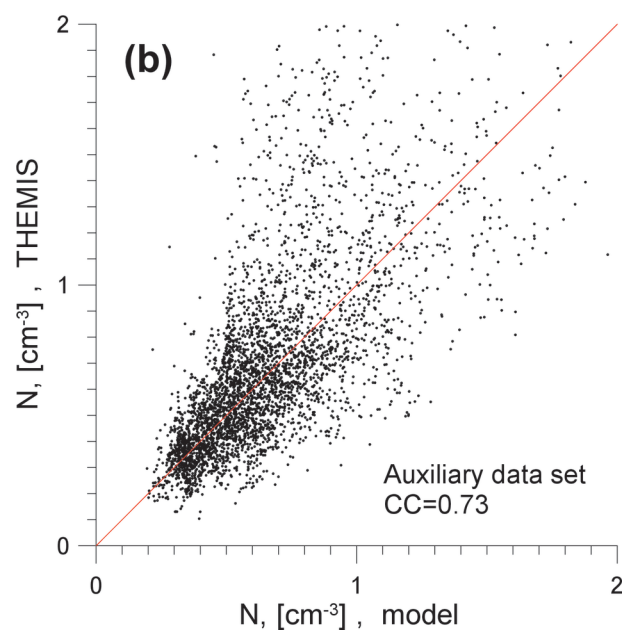
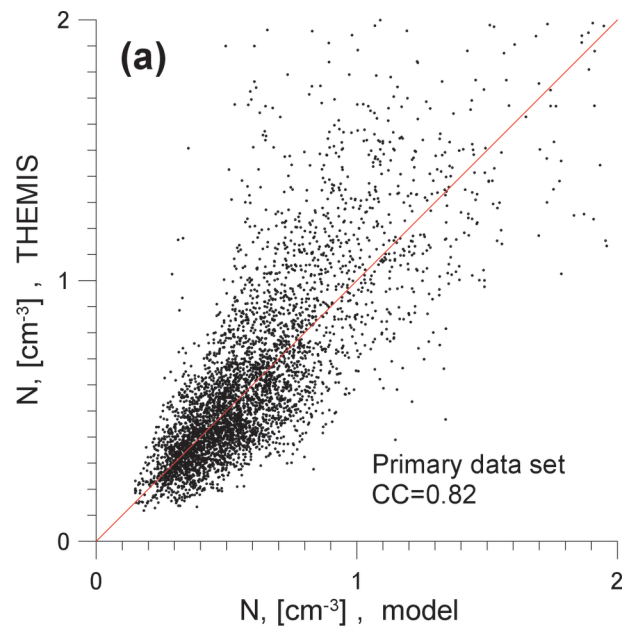
Auth

cript

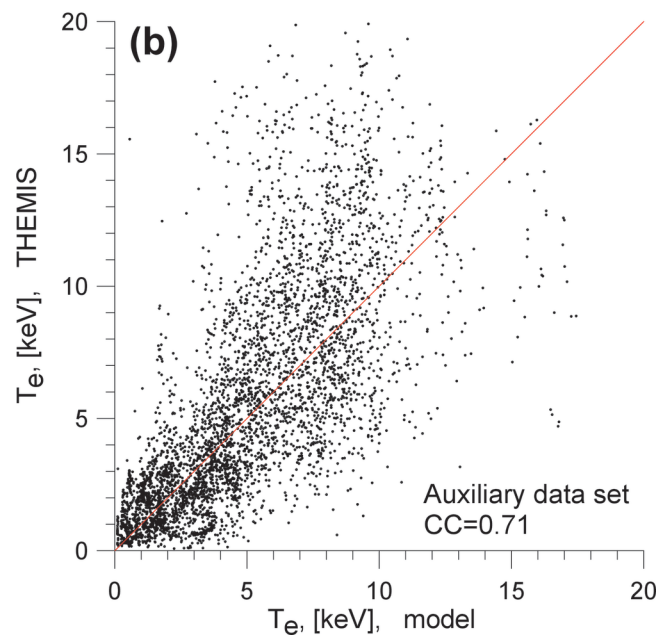
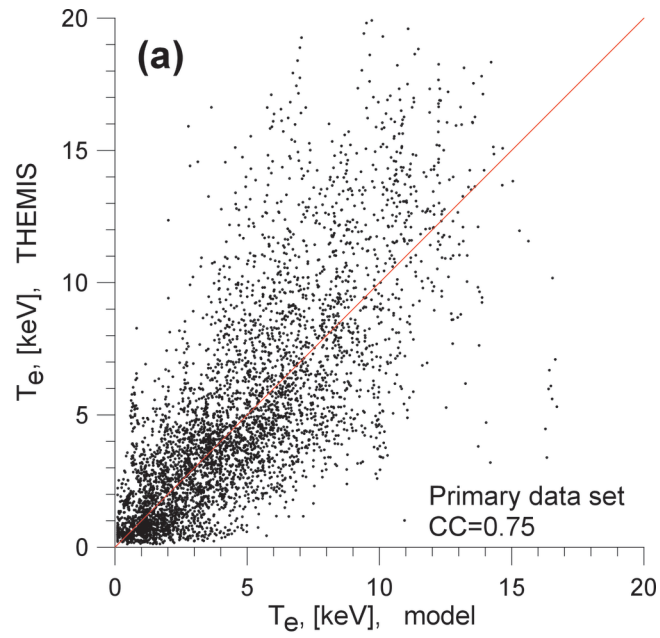


2016ja022947-f07-z-eps

Auth

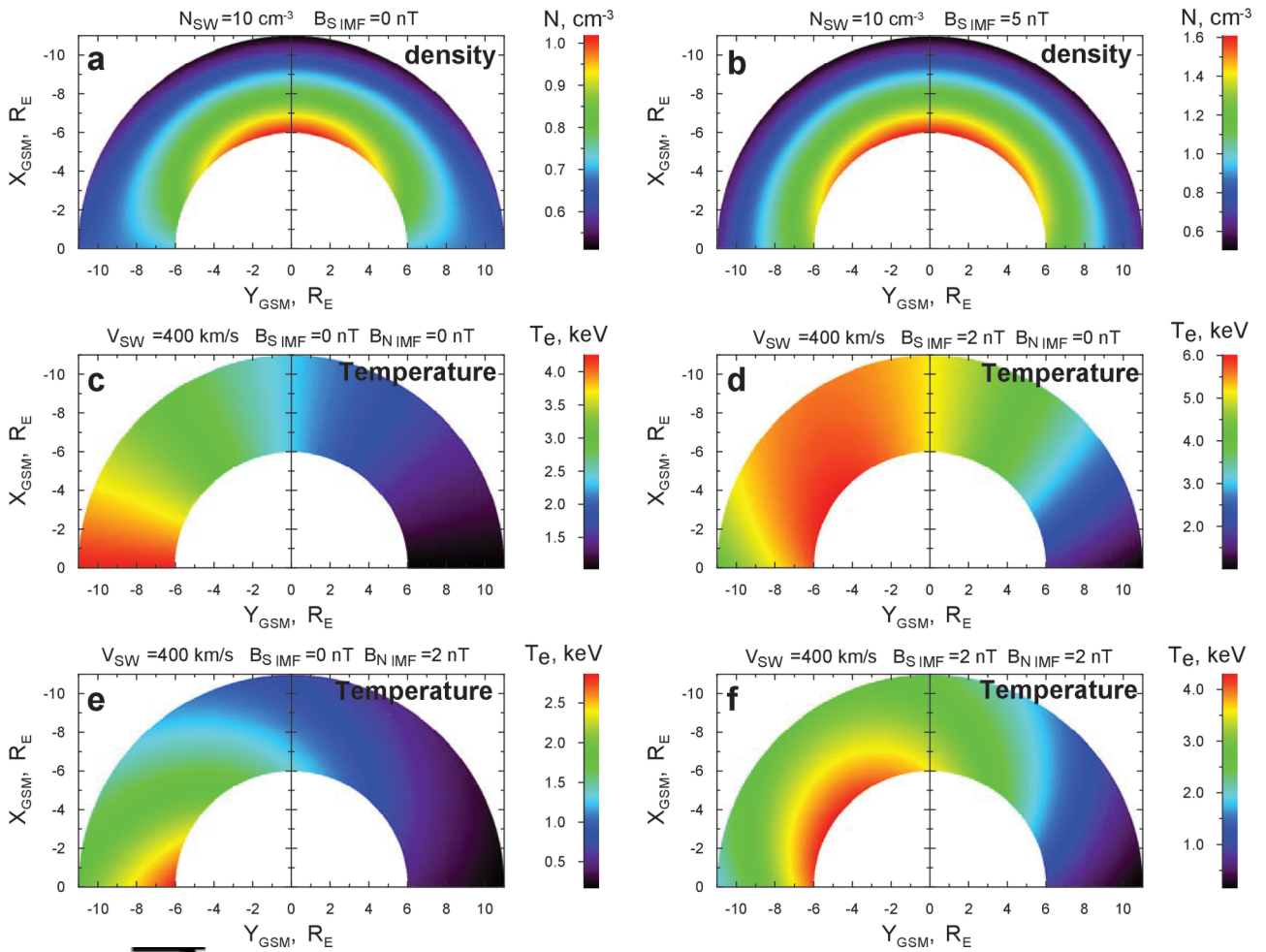


2016ja022947-f08-z-eps



2016ja022947-f09-z-.eps

ipt



AU

2016ja022947-f10-z-.eps